

1 **Evaluating Processing Choices for the Geodetic**
2 **Estimation of Earth Orientation Parameters with**
3 **Numerical Models of Global Geophysical Fluids**

4 **R. Dill¹, H. Dobsław¹, H. Hellmers², A. Kehm³, M. Bloßfeld³, M. Thomas¹, F.**
5 **Seitz³, D. Thaller², U. Hugentobler⁴, E. Schönemann⁵**

6 ¹Helmholtz Centre Potsdam GFZ German Research Centre for Geosciences, Section 1.3 Earth System
7 Modelling, Telegrafenberg, 14473 Potsdam, Germany

8 ²Federal Agency for Cartography and Geodesy BKG, Richard-Strauss-Allee 11, 60598 Frankfurt,
9 Germany

10 ³Deutsches Geodätisches Forschungsinstitut (DGFI-TUM), Technical University of Munich, Arcisstraße
11 21, 80333 Munich, Germany

12 ⁴Fachgebiet Satellitengeodäsie (FSG), Technical University of Munich, Arcisstraße 21, 80333 Munich
13 Germany

14 ⁵European Space Operations Centre ESOC, Navigation Support Office, 64293 Darmstadt, Germany

15 **Key Points:**

- 16 • Inter-technique combination of intra-technique EOPs at solution-, normal equation-
17 , and observation-level.
18 • Benchmarking of geodetic EOP time series against model-based effective angu-
19 lar momentum functions.
20 • Inconsistent terrestrial reference frames lead to spurious high-frequency signals in
21 combined EOPs.

Corresponding author: R. Dill, dill@gfz-potsdam.de

Abstract

Different Earth orientation parameter (EOP) time series are publicly available that typically arise from the combination of individual space geodetic technique solutions. The applied processing strategies and choices lead to systematically differing signal and noise characteristics particularly at the shortest periods between 2 and 8 days. We investigate the consequences of typical choices by introducing new experimental EOP solutions obtained from combinations at either normal equation level processed by DGFI-TUM and BKG, or observation level processed by ESA. All those experiments contribute to an effort initiated by ESA to develop an independent capacity for routine EOP processing and prediction in Europe. Results are benchmarked against geophysical model-based effective angular momentum functions processed by ESMGFZ. We find, that a multi-technique combination at normal equation level that explicitly aligns a priori station coordinates to the ITRF2014 frequently outperforms the current IERS standard solution 14C04. A multi-GNSS-only solution already provides very competitive accuracies for the equatorial components. Quite similar results are also obtained from a short combination at observation level experiment using multi-GNSS solutions and SLR from Sentinel-3A and -3B to realize space links. For ΔUT1 , however, VLBI information is known to be critically important so that experiments combining only GNSS and possibly SLR at observation level perform worse than combinations of all techniques at normal equation level. The low noise floor and smooth spectra obtained from the multi-GNSS solution nevertheless illustrates the potential of this most rigorous combination approach so that further efforts to include in particular VLBI are strongly recommended.

1 Introduction

The orientation of the solid Earth with respect to the celestial reference frame needs to be precisely known for a number of applications including ground-based astrometric observations, communication with satellites including probes in deep space, and also global navigation satellite systems (GNSS) nowadays used for the positioning of sometimes rapidly and even autonomously moving objects on the ground or in the air. Space geodetic techniques such as GNSS at permanent stations, Very Long Baseline Interferometry (VLBI), Satellite Laser Ranging (SLR), or Doppler Orbitography and Radio-Positioning Integrated by Satellite (DORIS) provide information about time-variations in the position of the terrestrial pole (polar motion), the phase angle of Earth's rotation ΔUT1 expressed as the difference between Universal Time (UT1) and the Coordinated Universal Time (UTC), and the celestial pole offsets (nutation). Those five (time-variable) parameters are conventionally referred to as Earth Orientation Parameters (EOP). The drift parameters related to each of these EOP can be also determined by the space-geodetic techniques. Therein, ΔLOD plays an important role related to the spin rate of the Earth.

Due to the advent of more precise sensors, denser measurement networks, and the availability of (at least partly) redundant observation techniques, the precision of space geodesy has improved over the most recent decades. Commonly, the available sensor data is combined into intra-technique EOP solutions in a least-squares sense to arrive at best possible solutions with minimal errors. A number of intra-technique EOP solutions is subsequently combined by various approaches to arrive at one single EOP time series. However, in view of the high internal precision of the individual techniques it becomes increasingly important to enforce consistency among the different techniques to avoid the introduction of spurious artifacts. This includes in particular all aspects of the realization of the terrestrial reference system. Similar attention should be devoted to geophysical background models required to process individual observations like, e.g., solar radiation pressure effects on individual satellites, or ocean tide models including ocean tidal loading that affect space geodetic observations in numerous and typically highly systematic ways. A more rigorous way for the combination of the individual space-geodetic technique solutions would be the combination at the normal equation (NEQ) level of the

74 Gauss-Markov model before solving for EOP. Ideal from a theoretical perspective would
 75 be the combination at observation level using one single software with identical parametriza-
 76 tions and background models to invert the observations from all techniques at once. So
 77 far, no publicly available EOP time series is applying any of the latter two approaches.

78 Polar motion and ΔLOD are governed mainly by terrestrial processes associated
 79 with the re-distribution of masses of the near-surface geophysical fluids. Variations in
 80 ΔLOD are largely dominated by zonal tropospheric winds (Salstein, 1993), whereas at-
 81 mospheric surface pressure and ocean dynamics are rather equally important for the ex-
 82 citation of high-frequency polar motion variations (Ponte & Ali, 2002). On seasonal time-
 83 scales, large-scale variations in terrestrial water storage are dominant (Chen et al., 2012).
 84 On decadal-to-centennial periods, prominent contributors to polar motion are the low-
 85 frequency changes in the continental ice masses (Adhikari & Ivins, 2016), whereas ΔLOD
 86 is also affected by core-mantle coupling effects (Holme & De Viron, 2013).

87 The quality of available models of global geophysical fluids relevant for the exci-
 88 tation of Earth orientation changes has increased tremendously in the more recent past.
 89 Atmospheric reanalyses produced by Meteorological Services like the European Centre
 90 for Medium-Range Weather Forecasts (ECMWF) are now routinely available (Dee et al.,
 91 2011). Particularly the mass component estimates of ocean and land hydrosphere mod-
 92 els have benefited from the availability of time-variable gravity field obtained with the
 93 GRACE mission (Göttl et al., 2019; Śliwińska et al., 2020). We therefore consider it nowa-
 94 days as a viable option to use a geophysical model data set as the reference against which
 95 different geodetic combination time series are compared. Although geophysical models
 96 cannot be considered as error-free, typical error sources of geodetic space techniques –
 97 like dependencies of the solar radiation pressure modeling on the satellite’s beta angle
 98 (elevation of the sun above the orbital plane) or spacecraft geometry – are not inherent
 99 in geophysical models, and therefore should become visible in such a comparison.

100 The paper is structured as follows: We collect three of the most commonly used
 101 EOP series that were calculated from a combination of different geodetic space techniques,
 102 and additionally introduce four experimental EOP combination series processed specifi-
 103 cally for this study within a project of the European Space Agency to improve EOP (Sec.
 104 2). Subsequently, we derive so-called geodetic excitation functions (GAM) out of the EOP
 105 that can be readily contrasted against geophysical effective angular momentum (EAM)
 106 functions (Sec. 3). Time series comparisons are provided in terms of root mean squared
 107 differences, Taylor plots, and explained variances for different frequency bands (Sec. 4).
 108 Since largest differences among the geodetic solutions are found for periods shorter than
 109 8 days, we specifically discuss spectra for those highest frequencies (Sec. 5). The paper
 110 closes with a discussion of the differences found in the geodetic solutions and some rec-
 111 ommendations for future improvements in the processing of combined geodetic EOP so-
 112 lutions.

113 For completeness, we note that the celestial pole offsets are largely governed by grav-
 114 itational attraction of different bodies of the solar system. Only a very tiny fraction of
 115 the nutation is caused by (seasonally modulated) diurnal tides in oceans and atmosphere
 116 that additionally deform the solid Earth by means of surface loading (Nastula & Śliwińska,
 117 2020). Albeit formally a part of the set of Earth Orientation Parameters, we entirely dis-
 118 regard celestial pole offsets in this study.

119 2 Selected EOP Time-Series

120 The Earth Orientation Center of the International Earth Rotation and Reference
 121 Systems Service (IERS) at Paris Observatory is the official provider (Bizouard, 2020)
 122 of daily estimates of polar motion and ΔUT1 . The excess length of day ΔLOD that is

123 related to the Earth’s rotation spin rate equals the difference of consecutive UT1-UTC
 124 estimates.

125 **2.1 C04-08: IERS 08C04**

126 The combination solution IERS 08C04 aligned to the ITRF2008 (called C04-08 in
 127 the remainder of this paper) results from a combination of intra-technique EOP series ob-
 128 tained from GNSS, VLBI, SLR, and DORIS (Gambis & Bizouard, 2009). One or two
 129 representative series from each technique are considered for the pole coordinates. For ΔUT1 ,
 130 the whole set of VLBI series available from the International VLBI Service for Geodesy
 131 and Astrometry (IVS) is taken into account, because no space-geodetic techniques other
 132 than VLBI is able to determine ΔUT1 in an absolute sense.

133 The intra-technique EOP series entering into the combination are made compat-
 134 ible by re-scaling the formal uncertainties and by re-aligning to both the International
 135 Celestial Reference Frame (ICRF) and the International Terrestrial Reference Frame (ITRF).
 136 Pole coordinates are smoothed by an epoch-dependent Vondrak-Filter (Vondrak, 1977)
 137 and are interpolated linearly to equidistant daily epochs. The trend of the ΔUT1 series
 138 derived from GNSS and SLR is aligned to the trend of ΔUT1 obtained from VLBI. The
 139 final series are again smoothed by Vondrák-Filtering to remove spurious variations likely
 140 introduced by the applied numerical procedures. Vondrák smoothing coefficients can be
 141 found at page 4 of the C04 description document ([ftp://hpiers.obspm.fr/iers/eop/](ftp://hpiers.obspm.fr/iers/eop/eopc04.08/C04_guide.pdf)
 142 [eopc04.08/C04_guide.pdf](ftp://hpiers.obspm.fr/iers/eop/eopc04.08/C04_guide.pdf)). Since C04-08 refers to the axis of the nowadays outdated
 143 ITRF2008, a slow degradation of the overall accuracy can be expected in particular for
 144 epochs in the year 2009 and later.

145 **2.2 C04-14: IERS 14C04**

146 The EOP combination procedure applied at Paris Observatory has been thoroughly
 147 upgraded to calculate a new series IERS 14C04 (Bizouard et al., 2017), called here C04-
 148 14. This EOP solution is re-aligned to the most recent ITRF, thereby also improving the
 149 numerical combination procedure by the introduction of more realistic weights for the
 150 intra-technique solutions. Updated Vondrák smoothing coefficients are reported in Ta-
 151 ble 3 in (Bizouard et al., 2019). Pole coordinates of C04-14 are now consistent with ITRF2014,
 152 whereas nutation offsets and ΔUT1 are aligned to the ICRF2 and ICRF3 before and af-
 153 ter the year 2019, respectively. The series C04-14 has been reprocessed back until 1962
 154 and is officially recommended by the IERS. It is updated two times per week, with an
 155 average latency of about 30 days. Differences to the previous solution C04-08 are as large
 156 as $50 \mu\text{s}$ in polar motion and $5 \mu\text{s}$ in ΔUT1 , and are primarily related to the selected
 157 terrestrial reference frame.

158 **2.3 JPL-Comb2018**

159 Earth Orientation Parameters are also processed at the Jet Propulsion Laboratory
 160 (JPL) of the National Aeronautics and Space Administration (NASA) in a manner that
 161 is fully independent from IERS. The so-called JPL-Comb2018 solution utilizes tracking
 162 data from Lunar Laser Ranging (LLR), the Global Positioning Satellite System (GPS),
 163 VLBI, SLR and historic optical astrometric observations by means of a Kalman Filter
 164 approach (Ratcliff & Gross, 2019). Rotational variations caused by solid Earth (Yoder
 165 et al., 1981) and ocean tides (Kantha et al., 1998) were removed from the ΔUT1 values
 166 prior to the combination and added back afterwards.

167 As the individual space geodetic techniques might use their own realizations of the
 168 terrestrial reference system when solving for EOP, e.g. EOP(IGS) 00 P 03 for the GNSS
 169 solutions provided by the International GNSS Service (IGS), both bias-rate corrections
 170 and uncertainty scale factors were determined for each single-technique EOP time se-

171 ries. Each individual series was compared to a combination of all other remaining series
 172 to estimate those parameters individually for each technique. The procedure was repeated
 173 iteratively until convergence among all considered single-technique solutions had been
 174 reached.

175 It should be noted that updates to this series are only published annually. For rou-
 176 tine applications JPL provides daily updates including short-term predictions by addi-
 177 tionally incorporating rapidly available observations such as the GPS and AAM forecasts
 178 from NCEP (<https://keof.jpl.nasa.gov>).

179 2.4 Experimental solutions by DGFI-TUM and BKG

180 The European Space Agency (ESA) is currently working towards establishing an
 181 independent capacity for calculating EOP out of multiple space geodetic data products
 182 processed within its Navigation Support Office (OPS-GN) at the European Space Op-
 183 erations Center (ESOC). An external team is currently being tasked with the develop-
 184 ment of a new combination software suitable for routine EOP estimation and prediction.
 185 This group consists of scientists from Deutsches Geodätisches Forschungsinstitut (DGFI-
 186 TUM) at the Technical University of Munich, Federal Agency for Cartography and Geodesy
 187 (BKG), Chair of Satellite Geodesy at the Technical University of Munich, Research Group
 188 Advanced Geodesy at the Technical University of Vienna, and the Earth System Mod-
 189 elling group at the Helmholtz Centre Potsdam GFZ German Research Centre for Geo-
 190 sciences (ESMGFZ). The work is in particular based on previous experience gained at
 191 DGFI-TUM as an IERS ITRS Combination Center (Seitz et al., 2012), and at BKG which
 192 is operating the IVS Combination Center jointly together with DGFI-TUM (Bachmann
 193 et al., 2016).

194 All input data to the combination software is provided in terms of technique-specific
 195 NEQs given in the Solution-Independent Exchange Format (SINEX) by ESA with the
 196 exception of the VLBI solutions (BKG). Before combination, the technique-specific NEQs
 197 undergo a set of pre-processing steps. Whereas GNSS, SLR, and DORIS already con-
 198 tain EOP parametrized at noon epochs, the VLBI-based EOP need to be transformed
 199 from session midpoints to the nearest noon epochs. The functional model of the Δ LOD
 200 parameter in the GNSS NEQs is expanded in order to account for a potential Δ LOD
 201 bias. In this study, we apply a fixed correction value of $-20 \mu\text{s}$ which is based on an anal-
 202 ysis (w.r.t. C04-14) of the ESA ESOC GPS+GALILEO LOD time series between 2016
 203 and 2019. Daily GNSS NEQs and session-wise VLBI NEQs are then accumulated to weekly
 204 technique-specific NEQs in order to match the weekly resolution of SLR and DORIS. The
 205 TRF datum for all techniques is kept by fixing all station coordinates to their a priori
 206 values, which ensures consistency between the estimated EOP and the a priori reference
 207 frame (Belda et al., 2017).

208 The combination of the weekly technique-specific NEQs to a common weekly NEQ
 209 is performed by summing up all NEQs with equal weights. Thereby, all technique-specific
 210 EOP at noon epochs are stacked to combined EOP at noon epochs. Parametrized are
 211 pole offsets, pole rates, Δ UT1, and Δ LOD. Each daily set of EOP at noon is transformed
 212 to the respective day boundaries as a pair of midnight offsets at 0h and 24h UTC, tak-
 213 ing into account the effect of tidal deformation on the Earth’s rotation in the transfor-
 214 mation of Δ UT1 and Δ LOD according to the IERS Conventions (Petit & Luzum, 2010).
 215 As described in Chapt. 8.1 of the conventions, all periods from 5 days to 18.6 years are
 216 considered for regularization. Afterwards, the pole offsets and Δ UT1 at the day bound-
 217 aries between consecutive days are stacked. As VLBI is the only space-geodetic technique
 218 that allows for the direct observation of Δ UT1, this procedure ensures that gaps between
 219 VLBI sessions are bridged with Δ LOD information from the satellite techniques. Thus,
 220 the combined NEQ system is invertible without any further EOP constraints. After in-
 221 version, weekly solutions with full sets of EOPs at the day boundaries (eight different

epochs) are obtained. A time series of consecutive daily EOP estimates is subsequently generated by stacking the EOP values at the week boundaries at solution level, i.e., by calculating a weighted mean of the estimates. With that software and general processing strategy, the following two experiments E1 and E2 were performed.

2.4.1 *Experiment E1: Combination at NEQ-Level*

For Experiment E1, we use NEQs of GNSS and SLR solutions processed at the Analysis Center (AC) ESOC as regular contribution to the IGS, and to the International Laser Ranging Service (ILRS), respectively. In addition, 24-hour VLBI solutions are used from the IVS AC at DGFI-TUM, whereas VLBI Intensive solutions are taken from the IVS AC at BKG. Station coordinates as given in each intra-technique NEQ are not changed in this experiment. The main problem arising from this treatment of the routine products “as is” is that the ITRF realization to which the coordinates are referred changes over time, so the results have to be taken with care. Moreover, the NEQs provided by the IAG services do not necessarily contain station coordinates that are fully consistent with the ITRF2014, as technique-specific realizations of this TRF are used.

2.4.2 *Experiment E2: Combination at NEQ-Level aligned to ITRF2014*

In order to improve the consistency of the datum definition across all techniques, in the second experiment (E2) the station coordinates from ITRF2014 stations have been transformed to the ITRF2014 datum in advance. This procedure reduces datum inconsistencies for all stations given in the ITRF2014, but introduces some inconsistencies within the networks between ITRF2014 and non-ITRF2014 stations. However, these inconsistencies remain neglectable in the beginning of the processed period as the vast majority of sites processed is contained in ITRF2014. Later on, the inconsistencies become more relevant, as more stations not considered in the ITRF2014 are added especially to the GNSS network. Apart from the transformation of the a priori values before fixing the station coordinates, the combination approaches of experiments E1 and E2 are identical.

2.5 Experimental solutions by ESA

We hypothesize that consistency of the contributions from the different geodetic space-techniques is a key element to achieve a best-possible EOP accuracy. To achieve that goal, ESOC reprocessed archived observation data from the International Doris Service (IDS), IGS, and ILRS in a single homogenized solution (Otten et al., 2012) by using their own software NAVigation Package for Earth Orbiting Satellites (NAPEOS). This approach allows for the most rigorous combination of IDS, ILRS, and IGS reference frames by using space-ties. ESA is aiming for combining all space geodetic techniques on observation level (GNSS, SLR, DORIS and VLBI). However, to understand the impact of the different observation types, the solution is carefully extended by adding only one new observation type at a time. We use in this article two intermediate solutions.

2.5.1 *Experiment E3: Multi-GNSS solution as contribution to the third IGS reprocessing campaign*

The experiment E3 used in this study is identical with the ESA contribution to the third reprocessing campaign of the International GNSS Service (IGS). The EOP solution is based on the daily analysis of undifferenced pseudorange and carrier phase observations of 150 globally distributed multi-GNSS IGS tracking stations considering on average 31 GPS and 24 GLONASS satellites as well as, starting from 01/2014 also Galileo satellites. Initially only 4 Galileo satellites were included, but the number increased to 24 until 12/2018. As the data from the three constellations is jointly processed, with com-

mon receiver clocks estimates allowing for corresponding intersystem biases, the solutions can be considered as combined at the observation level with highest consistency. In view of a full set of EOPs, it is important to emphasize that especially VLBI is missing in experiment E3. Thus, ΔUT1 cannot fully be determined.

2.5.2 *Experiment E4: Combination of GNSS and SLR at observation level*

We introduce also a very recent solution that combines GNSS observations with tracking data of Sentinel-3A and Sentinel-3B as low Earth orbiters for this space link. Both GNSS and SLR observations to those satellites are considered. The data is rigorously combined at observation level. So far just 12 months of data from experiment E4 were completed so that a full evaluation of this series by means of model-based EAM is not possible. Therefore, we will discuss E4 in Sec. 5 only. Please note that ΔUT1 can be expected to be determined similarly poorly as in experiment E3.

3 Effective Angular Momentum Functions

Changes in the orientation of the solid Earth are conveniently studied by applying the principle of conservation of angular momentum in the whole Earth system including its surrounding fluid layers. Relevant are both the instantaneous mass distribution (matter terms) and the relative angular momentum changes associated to winds and currents (motion terms). Globally integrated angular momentum changes are multiplied with empirically derived parameters to account for the actual rheology of the Earth including, e.g. the anelasticity of the mantle, the partly de-coupled rotation of the core, and the associated equilibrium response of the oceans (Brzeziński, 1992; Gross, 2007). It is important to note that in contrast to EOP time series, EAMs are free of the dominating Chandler wobble in the equatorial components.

Globally integrated changes in angular momentum of each of the sub-systems can be described by effective angular momentum functions (EAM) derived from individual global numerical models. Customarily, those contributions are named as atmospheric angular momentum (AAM), oceanic angular momentum (OAM), and hydrological angular momentum (HAM). The additional effect of a time-variable barystatic sea-level in response to a net-transfer of water mass from the land into the ocean is sometimes assumed to be part of the OAM, but sometimes also kept separated and labelled as sea-level angular momentum (SLAM).

3.1 ESMGFZ: Geophysical Model-Based EAM

The various geodetic solutions will be evaluated against a model-based EAM time series provided by the Earth System Modelling group at Deutsches GeoForschungsZentrum (ESMGFZ). The daily updated non-tidal EAM data is given in terms of dimensionless effective angular momentum functions of the matter and motion terms individually for the Earth's sub-systems atmosphere, ocean, and terrestrial water storage. The underlying mass redistribution for atmospheric surface pressure is taken from the European Centre for Medium-Range Weather Forecasts (ECMWF), ocean bottom pressure and vertically integrated ocean currents are simulated with the Max-Planck Institute for Meteorology Ocean Model (MPIOM) (Jungclaus et al., 2013), and terrestrial water storage is simulated with the Land Surface and Discharge Model (LSDM) (Dill, 2008). Please note that contributions of the 12 most prominent tidal frequencies have been removed from atmosphere and ocean. Additional contributions arising from major earthquakes (Chao & Gross, 1995; Yun, 2019), electromagnetic jerks at the core-mantle boundary (Ron et al., 2019), or glacial processes in the continental ice-sheets (Mitrovica & Wahr, 2011) present in the geodetic observations are not covered by this model-based data-set. As

317 the geophysical models do only represent mass variations and mass exchange but pro-
 318 vide no access to the absolute atmospheric, oceanic, and terrestrial water masses, a long-
 319 term mean (2003–2014) has been already removed from the EAM products. Further in-
 320 formation on the product is provided via the web-page [http://esmdata.gfz-potsdam](http://esmdata.gfz-potsdam.de:8080/repository)
 321 [.de:8080/repository](http://esmdata.gfz-potsdam.de:8080/repository) and in the product description document (Dobslaw & Dill, 2018).

322 3.2 Geodetic Angular Momentum

323 To obtain excitation functions out of observed EOP, the Liouville equation

$$\dot{p} - i\sigma_c p = -i\sigma_c \chi, \quad (1)$$

324 with pole coordinates $p = p_1 + ip_2$ and complex Chandler frequency $\sigma_c = 2\pi(1 +$
 325 $i/2Q)/T_c$ is de-convoluted (Wilson & Vicente, 1990) to transform pole coordinates into
 326 so-called geodetic angular momentum functions (GAM) $\chi = \chi_1 + i\chi_2$. We use a Chan-
 327 dler period of $T_c = 434.2$ days with a damping of $Q = 100$, which is consistent with the
 328 parametrization of the rotational deformation applied in the model-based EAM calcu-
 329 lations. The axial component χ_3 follows from

$$\frac{d}{dt}(\text{UT1} - \text{UTC}) = -\Delta\text{LOD} = \chi_3 \cdot 86400 \quad (2)$$

330 GAM are available for every day since 1962. Those GAM should be therefore un-
 331 derstood as the excitation required to change Earth orientation in a way as it is observed
 332 by space geodesy. Effects of long-period tides were removed from ΔLOD as recommended
 333 in the IERS conventions (Petit & Luzum, 2010) to make χ_3 comparable to the non-tidal
 334 EAM from ESMGFZ.

335 As an introductory example, we show time-series of GAM derived from JPL-Comb2018
 336 together with the sum of model-based EAM functions from ESMGFZ (Fig. 1). We note
 337 that model-based EAM explain almost 90 % of the intra-annual signal in χ_3 , which is
 338 related to the dominance of seasonal variations in zonal tropospheric winds that are very
 339 well captured by present-day atmospheric reanalyses. For the equatorial components,
 340 residuals are much larger (approximately 50 %) with both strong high-frequency vari-
 341 ability and a distinct long-term trend. The equatorial components are rather sensitive
 342 to mass distributions in polar regions with both strong variability in the wind-driven ocean
 343 dynamics and slow mass loss of ice-sheets and glaciers. Nevertheless, a considerable frac-
 344 tion of the signal seen by JPL-Comb2018 is explained by the model-based EAM so that
 345 it is sensible to use the geophysical model as a reference to evaluate the different geode-
 346 tic solutions.

347 4 Time Series Analysis

348 GAM series are calculated according to Sect. 3.2 from all EOP series introduced
 349 in Sect. 2. Except for experiment E4, all series are available to us with daily sampling
 350 from January 2009 to April 2019. EAM are taken as sum of AAM, OAM (both sampled
 351 from 3h sampling to the daily epochs of GAM), HAM, and SLAM. A third-order But-
 352 terworth filter with varying cut-off periods is applied to split all time-series into three
 353 frequency bands: (1) 2 – 8 days, (2) 8 – 20 days, and (3) 20 – 100 days. In addition, also
 354 the (4) combined band of 2 – 100 days, and the (5) unfiltered series that includes all pe-
 355 riods above 2 days are considered. We calculate various metrics commonly applied in time
 356 series analysis to quantify the correspondence of GAM and EAM. In particular, we use
 357 root mean squared differences (RMSD), standard deviations (STD), the Pearson corre-
 358 lation coefficient (CORR), and explained variances (EXVAR).

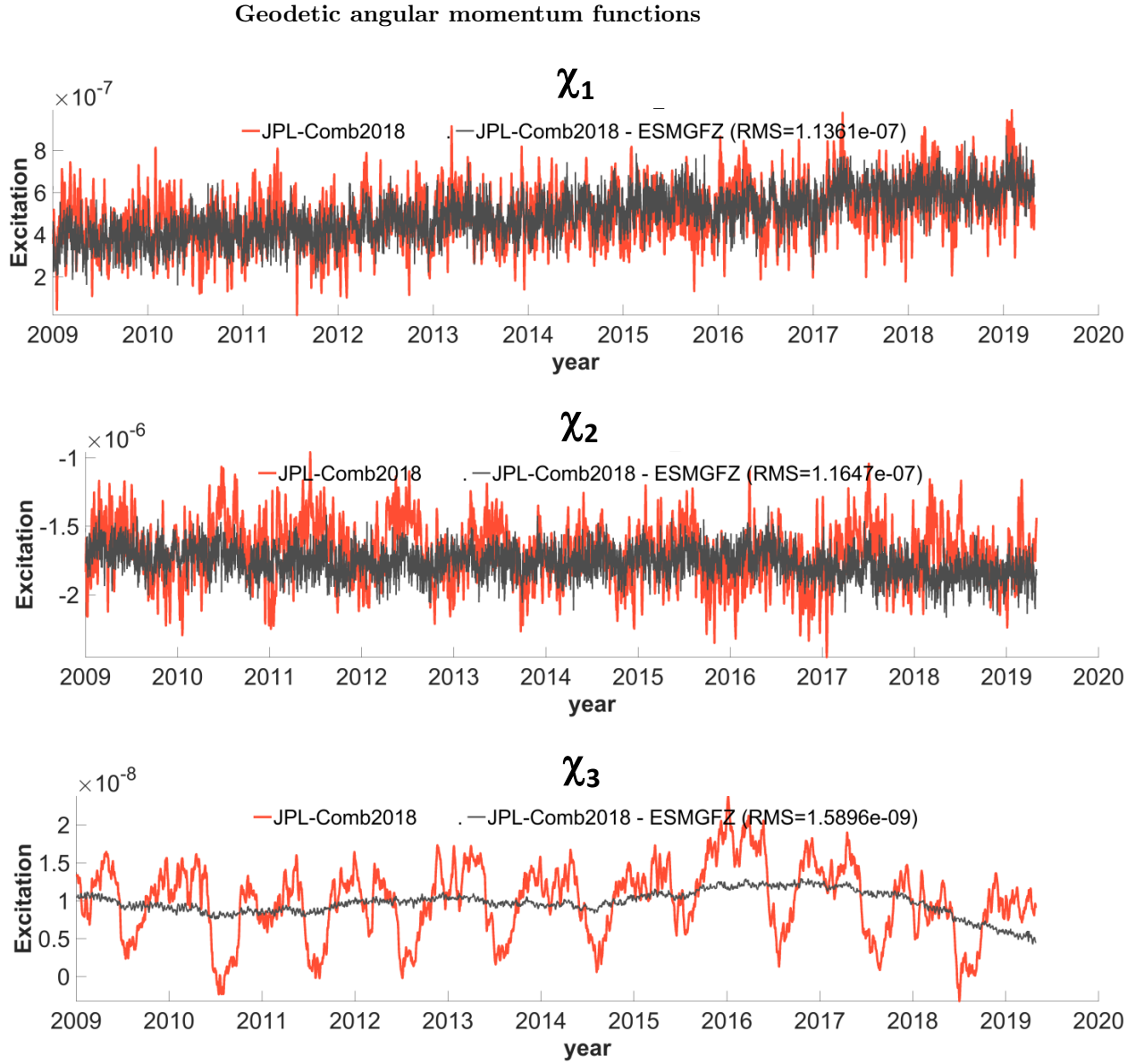


Figure 1. Geodetic angular momentum functions GAM from JPL-Comb2018 (red) and the residual after subtracting the model-based EAM from ESMGFZ (grey), for χ_1 (top), χ_2 (middle), and χ_3 (bottom). Excitation functions GAM and EAM are unitless.

Root mean squared differences (RMSD)

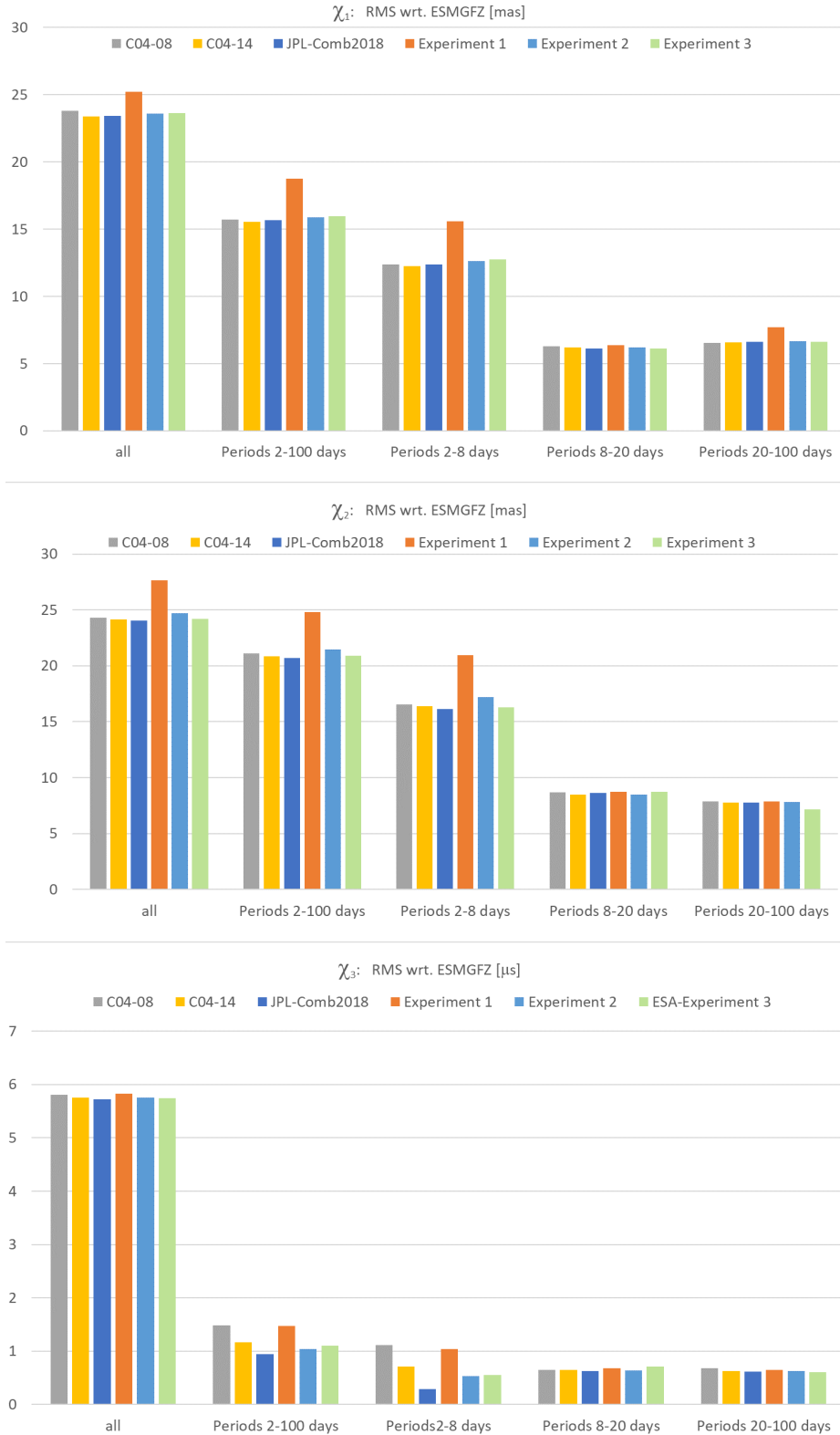


Figure 2. Root mean squared differences (RMSD) between geodetic angular momentum time-series GAM of different EOP solutions and the model-based EAM from ESMGFZ, for χ_1 (top), χ_2 (middle), and χ_3 (bottom). For better comparison, units are transformed into milliarcseconds [mas] for the equatorial components χ_1 and χ_2 , and in microseconds [μ s] for the axial component χ_3 .

359 Root mean squared differences (RMSD) quantify the residual variability after sub-
 360 tracting ESMGFZ EAM from any of the GAM series, reduced by their mean offset over
 361 the analyzed period (Fig. 2). For the periods above 8 days, we find very consistent re-
 362 sults across the six GAM series considered. The only exception is the experiment E1,
 363 which has 5 % higher RMSD in χ_1 . Differences among the geodetic series are more pro-
 364 nounced at the highest frequencies: For the pole, E1 fits rather poorly to ESMGFZ when
 365 compared to the other solutions. For ΔLOD , both E1 and C04-08 have the largest mis-
 366 fit, whereas both experiments E2 and E3 are even slightly better than C04-14. In all com-
 367 ponents, JPL-Comb2018 provides the best fit to the model, and the largest margin with
 368 respect to the competing geodetic series is found in the third component.

369 To properly interpret the RMSD, it should be viewed in relation to the standard
 370 deviations of the two time series involved. It should be noted that the RMSD can be read-
 371 ily calculated from STDs and CORR according to

$$\text{RMSD}_{t,\text{ref}}^2 = \text{STD}_t^2 + \text{STD}_{\text{ref}}^2 - 2 \cdot \text{STD}_t \cdot \text{STD}_{\text{ref}} \cdot \text{CORR}_{t,\text{ref}} \quad (3)$$

372 where indices t and ref denote the time series to be tested and the reference time
 373 series, respectively. That relation equals the law of cosines where STD_{ref} and STD_t
 374 are the length of the sides of a triangle, and $\text{CORR}_{t,\text{ref}}$ referring to the cosine of the angle
 375 between those sides. Hence, $\text{RMSD}_{t,\text{ref}}$ is the length of the third side of the triangle vis-
 376 à-vis to the correlation angle. Eq. 3 therefore provides a geometrical relationship between
 377 the different metrics that can be used to display all three metrics jointly within a so-called
 378 Taylor diagram (Taylor, 2001). The Taylor diagram shows the agreement of any time
 379 series with a reference series not only by means of the RMSD, but provides a synopsis
 380 with the corresponding STD and CORR values. In principle, we are looking for results
 381 with a low RMSD, a STD similar to the reference series, and a high CORR coefficient.

382 In the following, we present Taylor diagrams that not only display results for the
 383 different GAM series (each by a separate color), but also for the different filters applied
 384 (each by a separate marker). For every category, the STD of the geophysical model-based
 385 time series ESMGFZ is given at the axis of abscissa as the reference point. The Euclidean
 386 distance from the reference point to the marker ($\text{STD}_t, \text{CORR}_t$) of an individual series
 387 gives the RMSD_t that is equal to the values given in the bar plots of Fig. 2.

388 For both equatorial components (Fig. 3, top row), we generally find a good cor-
 389 respondence of all GAM series with the modelled EAM. Results for 20 – 100 days (stars)
 390 are very close to each other, and also the results for 8 – 20 days are quite similar for all
 391 six geodetic series considered. For the shortest periods below 8 days (squares), we find
 392 a substantially larger spread: C04-08 and C04-14 are still very close to each other, with
 393 slightly smaller RMSD and slightly higher correlation for the more recent series from IERS.
 394 JPL-Comb2018 has a notable smaller STD than C04, which nevertheless does not always
 395 lead to a smaller RMSD misfit. We also find a huge reduction in STD for E2 when com-
 396 pared to E1: since both experiments only differ in the treatment of the station coordi-
 397 nates (as given in the SINEX files for E1; taken from ITRF2014 where possible for E2),
 398 this result clearly underlines the importance of precise a priori coordinates for the de-
 399 termination of EOP.

400 We further note that experiment E3 always has the smallest STD from all geode-
 401 tic time-series considered. We recall that this is a multi-GNSS solution only and VLBI,
 402 SLR, and DORIS observations are not included in this experiment. We nevertheless note
 403 that correlation and also RMSD are already quite competitive with respect to the other
 404 geodetic series. This indicates that pole coordinates are indeed very well determined from
 405 GNSS information alone. It is important to recall the (relatively) good performance of
 406 E3 might arise from the fact that all geodetic solutions except E3 have to deal with dif-
 407 ferent parametrizations for the station positions adopted by the various Analysis and Tech-

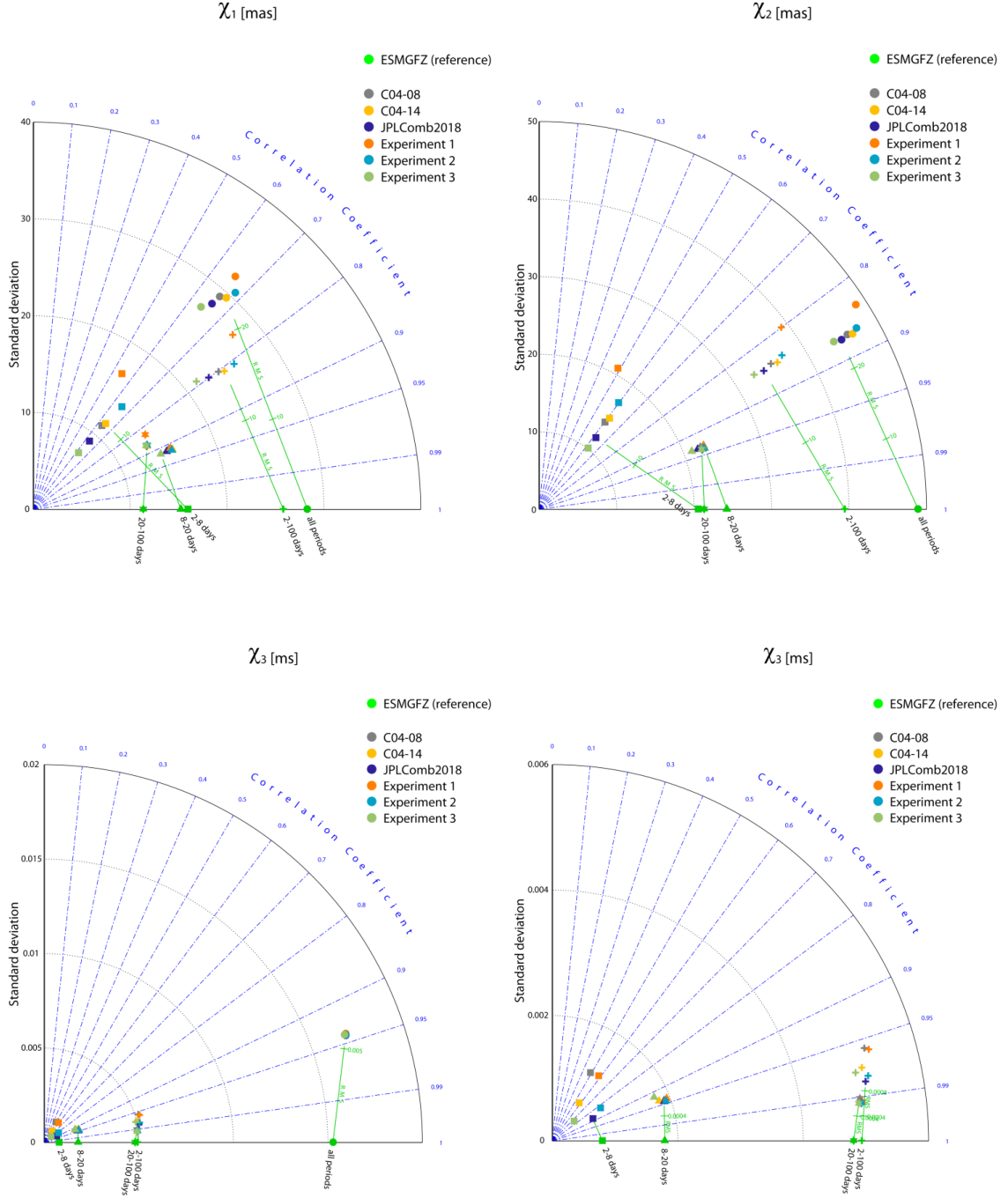
Taylor diagrams (STD-CORR-RMSD)


Figure 3. Standard deviation (STD) and correlation (CORR) of geodetic angular momentum time-series GAM derived from different EOP solutions compared to the model-based EAM of ESMGFZ for χ_1 (top-left), χ_2 (top-right), χ_3 for all frequency bands (bottom-left), and a zoom-in for χ_3 to standard deviations smaller than 0.006 ms (bottom-right). The mis-fit between GAM and EAM is given as root mean squared error RMSD by the distance between point of the GAM (STD/CORR) and the reference point for the EAM (STD/CORR=1). Different markers represent the results for 2 – 8 days (squares), 8 – 20 days (triangles), 20 – 100 days (stars), 2 – 100 days (pluses), and all periods (dots). For better comparison, units are transformed into milliarcseconds [mas] for the equatorial components χ_1 and χ_2 , and in microseconds [μ s] for the axial component χ_3 .

408 nique Center which have a direct impact on the EOP solutions (Bloßfeld et al., 2014).
 409 For completeness, we also present the results for the band 2 – 100 days (pluses) and the
 410 unfiltered series (dots). The results basically reflect the findings of the weekly band and
 411 do not need to be reiterated here.

412 For the axial component (Fig. 3, bottom row), we find again very consistent re-
 413 sults across all geodetic series for the lower frequencies and significant scatter only for
 414 the shortest periods of 2 – 8 days. For this component, C04-14 is a substantial improve-
 415 ment over the older series C04-08 with much reduced STD of the series, leading to both
 416 a smaller RMSD and a higher CORR with the geophysical EAM. This improvement is
 417 mirrored by the difference between E1 and E2, highlighting again the importance of a
 418 consistent terrestrial reference frame for EOP estimation. E3 has again the smallest STD
 419 of all series considered, but CORR and RMSD are much worse than experiment E2, thereby
 420 strongly underlining the well-known importance of VLBI for the determination of ΔUT1
 421 and consequently ΔLOD . The best results in this comparison are obtained with JPL-
 422 Comb2018, where a similarly small STD is connected with CORR and small RMSD, in-
 423 dicated that a good compromise has been found in this series to suppress high-frequency
 424 noise while retaining the relevant short-period signals. As for the equatorial components,
 425 the results for the other frequency bands are also included in the plots for completeness,
 426 but do not provide additional insights.

427 As an additional evaluation metric not captured by Taylor plots, we define the ex-
 428 plained variance (EXVAR) as

$$\text{EXVAR}_{t,\text{ref}} = 1 - \frac{\text{STD}_{\text{err}}^2}{\text{STD}_{\text{ref}}^2} \cdot 100\% \quad (4)$$

429 with $\text{STD}_{\text{err}}^2$ as the variance of the unexplained signal, that is the difference be-
 430 tween the time series and its reference. Note that this quantity is also sometimes called
 431 coefficient of determination in the statistical literature. For identical time series, EXVAR
 432 equals 100 %, and for time series not fitting at all it might even become negative.

433 For the polar motion excitations χ_1 and χ_2 , EXVAR reaches values between 30 %
 434 and 75 % depending on the period band considered (Fig. 4). Differences among the six
 435 geodetic solutions are very small apart from the shortest periods between 2 and 8 days.
 436 Here, four series have a similar level of EXVAR for both χ_1 and χ_2 , whereas experiment
 437 E1 has very small and barely positive values only. As the a priori station coordinates were
 438 kept as given in the intra-technique NEQs and it is not mandatory that the technique-
 439 specific realizations of the terrestrial reference system are aligned to each other, station
 440 coordinates in E1 might differ among the techniques. Those differences in the station
 441 coordinates were eliminated in E2, which consequently does not contain anymore such
 442 spurious high frequency signals that almost entirely mask the real geophysical signal con-
 443 tained in the geodetic observations. Best results in this comparison are again obtained
 444 by JPL-Comb2018.

445 In the axial component χ_3 , the largest spread between the geodetic solutions is also
 446 found at the highest frequencies. C04-08 and E1 have largely negative explained vari-
 447 ances. C04-14 and E2 reveal significant improvements, with E2 outperforming C04-14
 448 by a substantial amount. It is interesting to note that the experiment E3 – the multi-
 449 GNSS solution – is also already outperforming C04-14 and lags only slightly behind E2.
 450 The best performance, however, is found again with JPL-Comb2018.

451 5 Spectral Analysis

452 We calculate amplitude spectra for all GAM time-series and their residuals against
 453 the model-based EAM from ESMGFZ. For the longer periods of the equatorial compo-

Explained Variances (EXVAR)

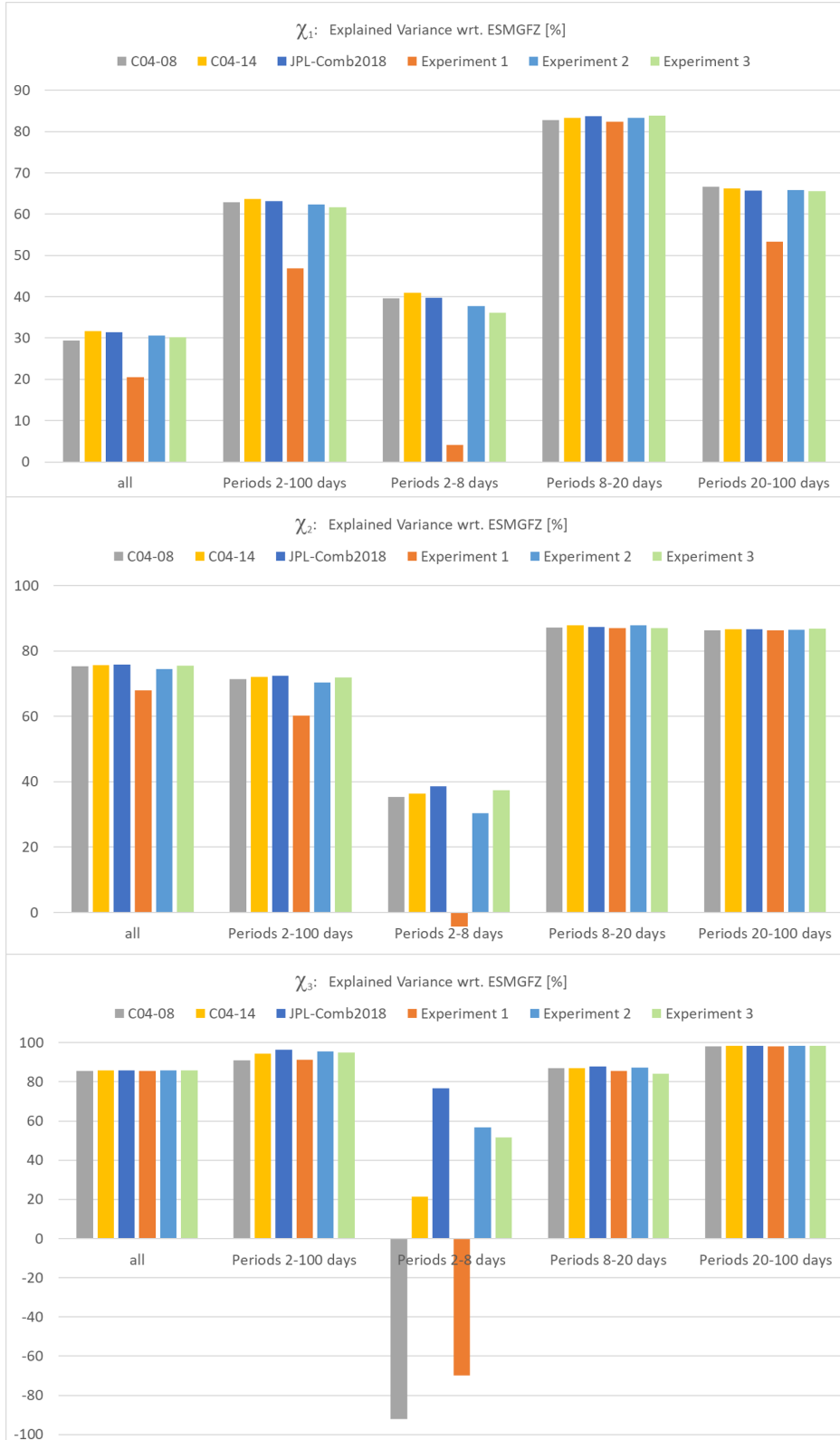


Figure 4. Explained variance (EXVAR) between geodetic angular momentum time-series GAM derived from different EOP solutions and model-based EAM from ESMGFZ, for χ_1 (top), χ_2 (middle), and χ_3 (bottom).

454 nents χ_1 and χ_2 , the residuals are dominated by a peak at 13.66 days not present in the
 455 EAM and possibly related to errors in the fortnightly tides (Ray et al., 2017). For the
 456 highest frequencies between 2 – 8 days, the spectra of the residuals against EAM differ
 457 substantially (Fig. 5, top and middle). We note very high variability and several signif-
 458 icant peaks in both C04-08 and also E1. Those peaks somewhat reduce for C04-14 and
 459 E2, but remain much larger than in JPL-Comb2018, where the energy found at the high-
 460 est frequencies is even lower than in the geophysical model. The experiment E3 instead
 461 has very little energy at the highest frequencies, which is between 2 and 3 days even smaller
 462 than in JPL-Comb2018. This is indeed interesting, since GNSS information with high
 463 temporal resolution has been ingested by the solution.

464 Results are quite similar also for the axial component χ_3 (Fig. 5, bottom). Promi-
 465 nent peaks are found in E1 and E2 at 7 days, which corresponds conspicuously to the cho-
 466 sen weekly NEQ accumulation interval. Less prominent peaks are also visible at the as-
 467 sociated overtones of 3.5 and 2.3 days. A similar characteristic is also seen in C04-08,
 468 but disappeared almost entirely in C04-14, which is known to suppress high-frequency
 469 variations by a strong smoothing algorithm. JPL-Comb2018 and also E3 instead do not
 470 contain such prominent peaks. For the highest frequencies, JPL-Comb2018 and E2 are
 471 approximately at the same level as ESMGFZ. It should be noted, however, that VLBI
 472 24-hour sessions are performed regularly twice a week (Mondays and Thursdays), which
 473 might contribute to the identified systematic. Moreover, no smoothing is applied in ex-
 474 periments E1 and E2. In contrast, the amplitude spectra of E3 calculated only from GNSS
 475 information reveals much smaller variability at those sub-weekly periods than predicted
 476 by the geophysical model, thereby clearly suggesting that important variability is not
 477 captured by the selected observing system configuration.

478 We also present here results from a preliminary combination of GNSS and SLR at
 479 observation level (Experiment E4), which is only available to us over 12 months from July
 480 2018 to June 2019 so that it could not be readily included into the analysis presented
 481 above. From the comparison of the residuals against Experiment E3 (Fig 6) it becomes
 482 obvious that the combination at observation level closely follows the multi-GNSS solu-
 483 tion with no obvious systematic differences. Differences between E4 and E3 are more than
 484 one magnitude smaller than the RMS of E3 to our reference ESMGFZ. Deviations of E4
 485 from E3 are also smaller than the deviations to other EOP series, e.g. JPL-Comb2018.
 486 However, because of the limited time span, we cannot conclude how far the addition of
 487 SLR improves the multi-GNSS EOP solution E3. Nevertheless, the results are generally
 488 encouraging and should further motivate ESA to extend the combination to a longer time
 489 span and include other geodetic techniques in order to allow for an in-depth analysis of
 490 EOP obtained from this most rigorous combination approach.

491 6 Summary and Conclusions

492 Three publicly available time series of terrestrial pole coordinates and ΔUT1 es-
 493 timates are augmented for this study by four experimental EOP series processed by DGFI-
 494 TUM, BKG and ESA that are all transformed into time-series of geodetic angular mo-
 495 mentum for contrasting against global geophysical fluid models. All geodetic series re-
 496 veal very similar variations for periods longer than a week, but show systematic differ-
 497 ences among each other at periods between 2 and 8 days. We therefore conclude that
 498 individual processing choices during the geodetic data analysis significantly affect the
 499 resulting EOP, in particular in the shortest periods.

500 A comparison against geophysical model-based excitation functions from ESMGFZ
 501 by means of various metrics (standard deviations, correlations, root mean squared dif-
 502 ferences, explained variances) documents the relative improvements achieved by the IERS
 503 with the transition from C04-08 to C04-14. The comparison also documents the supe-
 504 rior quality of JPL-Comb2018, even though it has to be kept in mind that the solution

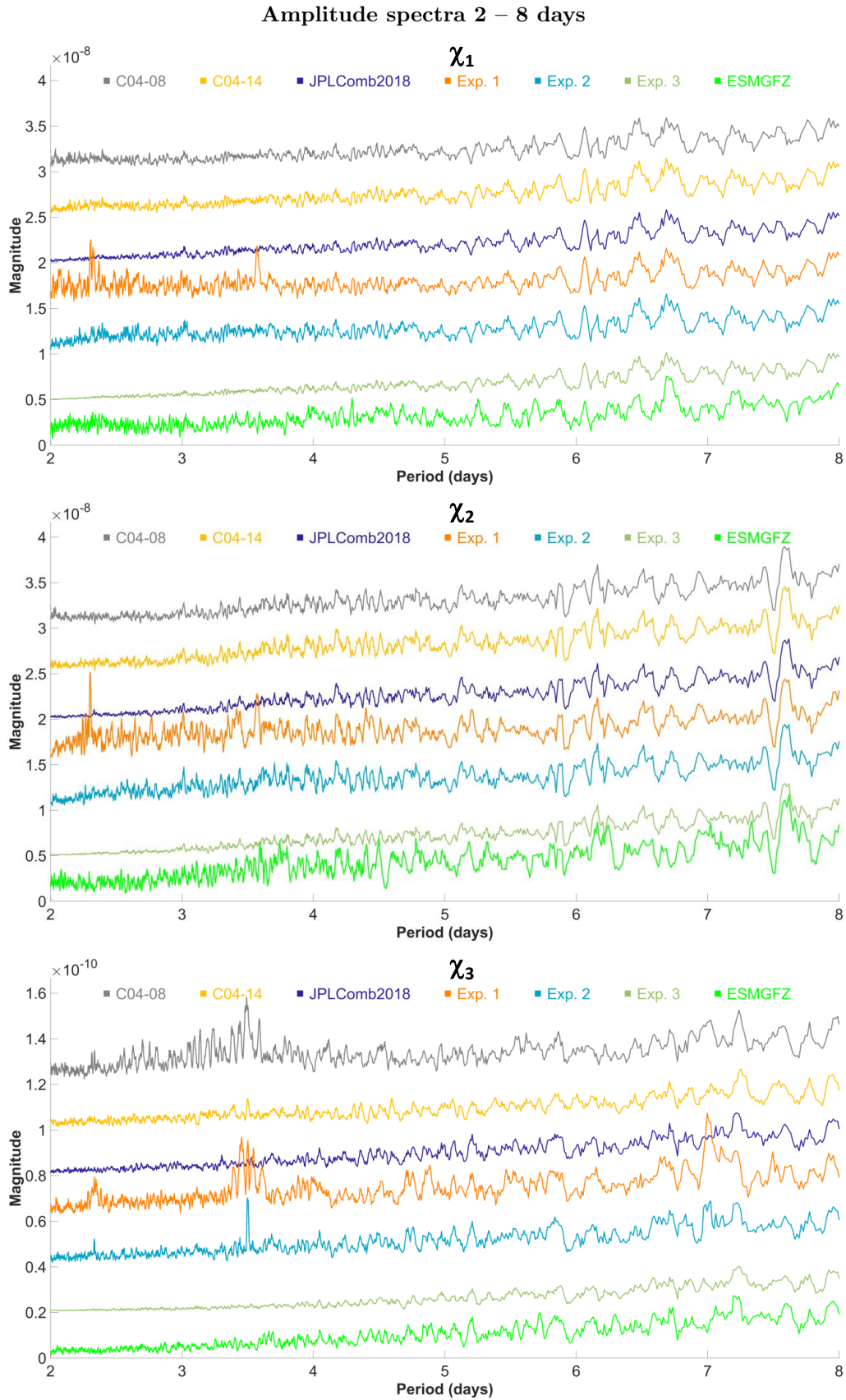


Figure 5. Amplitude spectrum of geodetic angular momentum time-series GAM derived from different EOP solutions and model-based EAM from ESMGFZ, for χ_1 (top), χ_2 (middle), χ_3 (bottom). For better readability the individual spectra were smoothed (5-point boxcar) and shifted by $0.5 \cdot 10^{-8}$ for χ_1 and χ_2 and $0.2 \cdot 10^{-10}$ for χ_3 . Excitation functions are unitless.

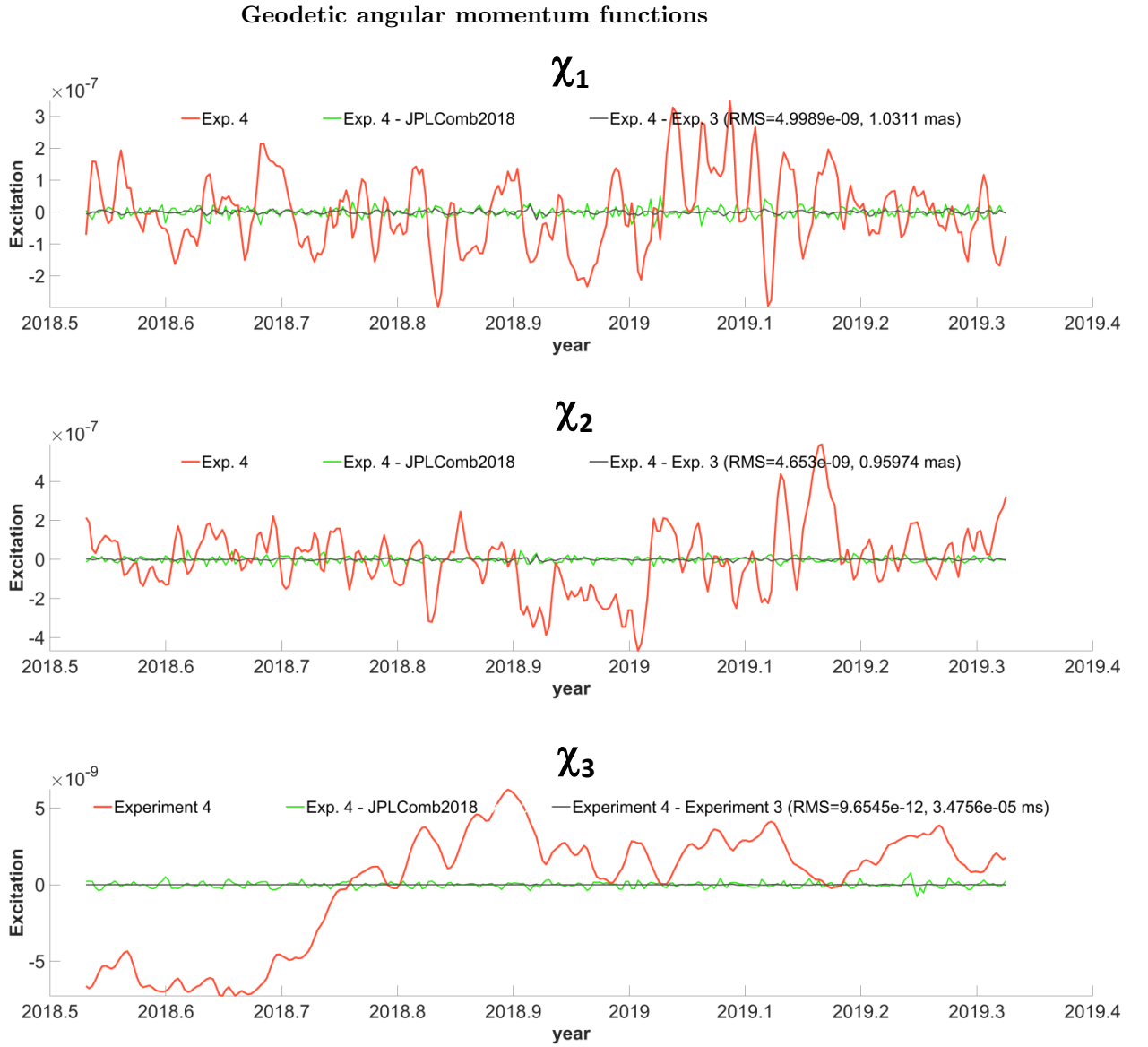


Figure 6. Geodetic angular momentum functions GAM from a combination of GNSS and SLR at observation level (Experiment E4; red) and residuals after subtracting experiment E3 (grey) and JPL-Comb2018 (green), for χ_1 (top), χ_2 (middle), and χ_3 (bottom). Excitation functions GAM and EAM are unitless. For better comparison with Fig. 2, RMS values are also given milliarcseconds [mas] for the equatorial components χ_1 and χ_2 , and milliseconds [ms] for the axial component χ_3 .

505 processed at JPL is not updated routinely but instead processed at once for a fixed pe-
506 riod of time. JPL-Comb2018 therefore should be regarded as the target accuracy that
507 should be aimed at with any EOP solution processed in an operational setting.

508 The new experimental EOP solutions processed by DGFI-TUM and BKG in an
509 operational setting agree well to the results obtained for the publicly available series. GAM
510 from a combination of data from different geodetic space techniques at normal equation
511 level that utilizes a priori coordinates as given in the SINEX files show spurious high-
512 frequency signals and corresponding poor fits to the geophysical EAM. In the underlying
513 EOP series the inconsistencies in the TRFs lead to high-frequency artifacts together
514 with several jumps followed by short-lasting drifts that cannot be removed easily when
515 combining EOP at the solution level. The quality of EOP obtained from a NEQ level
516 combination drastically increases when a priori coordinates are harmonized to a consist-
517 ent common reference frame. This solution generally even outperforms C04-14, thereby
518 demonstrating that the operational setting with input data from independent sources
519 combined at normal equation level, developed by DGFI-TUM and BKG, results in highly
520 competitive EOP estimates. Furthermore, it demonstrates that a combination at nor-
521 mal equation level is preferable to a combination at parameter level.

522 From a theoretical perspective, a combination at observation level that utilizes space
523 ties among the different geodetic techniques would be ideal for the processing of EOP.
524 Available to us are a multi-GNSS solution processed by ESA as a contribution to the
525 third reprocessing campaign of the IGS as well as preliminary results from a combina-
526 tion of Sentinel-3A and -3B with GNSS processed at ESOC. EOP from these solutions
527 are characterized by exceptionally low noise at the highest frequencies which lead to the
528 best fit with the geophysical model for the equatorial components among all operational
529 geodetic series considered. For the axial component, information from VLBI that is still
530 missing in those solutions leads to a degraded quality with respect to the results of a NEQ
531 level combination (including VLBI R1-, R4-, and Intensive-sessions) with ITRF2014 a
532 priori coordinates. Nevertheless, the achieved results for the pole are very promising, and
533 efforts should be expedited to also include VLBI and other techniques into this solution
534 type.

535 It should be emphasized that no additional smoothing has been applied to the EOP
536 series specifically processed for this study. Spurious effects identified in either the time
537 series or the spectral analysis as presented will now be analyzed further in order to iden-
538 tify possible causes for those artifacts. This might include the consequences of the se-
539 lected accumulation length of 7 days; the regular schedule of the 24-hours sessions (which
540 might be assessed by focusing on the epochs of the CONT campaigns, where significantly
541 more VLBI data is available); or the impact of certain background model choices includ-
542 ing the treatment of sub-daily tidal signals.

543 On a final note, the demonstrated ability to reliably identify consequences of in-
544 dividual processing choices on geodetic data products with the geophysical model-based
545 angular momentum functions demonstrate the tremendous improvement in accuracy in
546 those models achieved in the more recent past. For low frequency signals that allow for
547 the accumulation of geodetic observations over long periods of time and thus abundant
548 redundancy, geodetic estimates might be still safely regarded as a reference to bench-
549 mark numerical models against. For the higher frequencies with less observations and
550 a relatively higher impact of systematic errors, however, it would be prudent to evalu-
551 ate for each individual case if information readily provided by numerical models that in-
552 corporate information from various non-geodetic sources could be advantageously com-
553 bined with data from space geodesy to finally arrive at products with better external ac-
554 curacies.

555 **7 List of abbreviations**

AAM	Atmospheric Angular Momentum
AC	Analysis Center
BKG	Federal Agency for Cartography and Geodesy
CORR	Pearson correlation coefficient
DGFI-TUM	Deutsches Geodätisches Forschungsinstitut (DGFI-TUM), Technical University of Munich
DORIS	Doppler Orbitography and Radio-positioning Integrated by Satellite
EAM	Effective Angular Momentum functions
ECMWF	European Centre for Medium-Range Weather Forecasts
EOP	Earth Orientation Parameters
ERP	Earth Rotation Parameters
ESA	European Space Agency
ESMGFZ	Earth System Modelling Group at GFZ
ESOC	European Space Operations Center
EXVAR	Explained Variance
GAM	Geodetic Angular Momentum functions
GFZ	Helmholtz Centre Potsdam GFZ German Research Centre for Geosciences
GNSS	Global Navigation Satellite Systems
GPS	Global Positioning System
HAM	Hydrological Angular Momentum
IAG	International Association of Geodesy
ICRF	International Celestial Reference Frame
IGS	International GNSS Service
IERS	International Earth Rotation and Reference Systems Service
ILRS	International Laser Ranging Service
ITRF	International Terrestrial Reference Frame
IVS	International VLBI Service for Geodesy and Astrometry
JPL	Jet Propulsion Laboratory
LLR	Lunar Laser Ranging
LOD	Length-Of-Day
LSDM	Land Surface and Discharge Model
MPIOM	Max-Planck-Institute for Meteorology Ocean Model
NASA	National Aeronautics and Space Administration
NEQ	Normal Equation
OAM	Oceanic Angular Momentum
OPS-GN	Navigation Support Office at ESOC
RMSD	Root Mean Squared Difference
SINEX	Solution-Independent Exchange Format
SLAM	Sea-Level Angular Momentum
SLR	Satellite Laser Ranging
STD	Standard Deviation
UT1	Universal Time
UTC	Coordinated Universal Time
VLBI	Very Long Baseline Interferometry

557 **Acknowledgments**

558 The data-sets analyzed in this study are publicly available. The EOP time-series
559 C04-08 and C04-14 are provided via [https://www.iers.org/IERS/EN/DataProducts/](https://www.iers.org/IERS/EN/DataProducts/EarthOrientationData/eop.html)
560 [EarthOrientationData/eop.html](https://www.iers.org/IERS/EN/DataProducts/EarthOrientationData/eop.html). JPL-Comb2018 can be downloaded from [https://](https://keof.jpl.nasa.gov/combinations/2018/)
561 keof.jpl.nasa.gov/combinations/2018/. ESMGFZ angular momentum functions are
562 available at <http://esmdata.gfz-potsdam.de:8080/repository>.

563 This study emerged from a project funded by ESA intended to develop an inde-
564 pendent capacity to routinely process Earth orientation parameters at OPS-GN of ESOC

565 (ESA contract no. 4000120430/17/D/SR). RD processed the ESMGFZ EAM functions,
 566 performed the comparative analysis, and wrote the first manuscript draft together with
 567 HD. AK, MB, and HH computed the experimental EOP time-series. FS, MT, DT, and
 568 UH designed the study. ES initiated the study as the responsible ESA technical officer.
 569 All authors helped with interpreting the results and contributed to the final manuscript.

570 References

- 571 Adhikari, S., & Ivins, E. R. (2016). Climate-driven polar motion : 2003 – 2015. *Sci-*
 572 *ence Advances*, *2*(4), 1–11. doi: 10.1126/sciadv.1501693
- 573 Bachmann, S., Thaller, D., Roggenbuck, O., Lösler, M., & Messerschmitt, L. (2016,
 574 jul). IVS contribution to ITRF2014. *Journal of Geodesy*, *90*(7), 631–654. doi:
 575 10.1007/s00190-016-0899-4
- 576 Belda, S., Heinkelmann, R., Ferrándiz, J. M., Nilsson, T., & Schuh, H. (2017).
 577 On the consistency of the current conventional EOP series and the celestial
 578 and terrestrial reference frames. *Journal of Geodesy*, *91*(2), 135–149. doi:
 579 10.1007/s00190-016-0944-3
- 580 Bizouard, C. (2020). Earth Orientation Center. In D. Thaller & W. R. Dick (Eds.),
 581 *IERS Annual Report 2018*. Verlag des Bundesamts für Kartographie und
 582 Geodäsie, Frankfurt am Main, Germany.
- 583 Bizouard, C., Becker, O., & Richard, J. Y. (2017). Combined solution C04 for Earth
 584 Rotation Parameters consistent with International Terrestrial Reference Frame
 585 2014. *IERS Notice*(January), 1–15.
- 586 Bizouard, C., Lambert, S., Gattano, C., Becker, O., & Richard, J. Y. (2019).
 587 The IERS EOP 14C04 solution for Earth orientation parameters consis-
 588 tent with ITRF 2014. *Journal of Geodesy*, *93*(5), 621–633. doi: 10.1007/
 589 s00190-018-1186-3
- 590 Bloßfeld, M., Seitz, M., & Angermann, D. (2014). Non-linear station motions in
 591 epoch and multi-year reference frames. *Journal of Geodesy*, *88*(1), 45–63. doi:
 592 10.1007/s00190-013-0668-6
- 593 Brzeziński, A. (1992, feb). Polar motion excitation by variations of the effective an-
 594 gular momentum function: considerations concerning deconvolution problem.
 595 *Manuscr. Geod.*, *17*, 3–20.
- 596 Chao, B. F., & Gross, R. S. (1995). Changes in the Earth’s rotational energy in-
 597 duced by earthquakes. *Geophysical Journal International*, *122*(3), 776–783.
 598 doi: 10.1111/j.1365-246X.1995.tb06836.x
- 599 Chen, J. L., Wilson, C. R., & Zhou, Y. H. (2012). Seasonal excitation of polar mo-
 600 tion. *Journal of Geodynamics*, *62*(February 2002), 8–15. doi: 10.1016/j.jog
 601 .2011.12.002
- 602 Dee, D. P., Uppala, S. M., Simmons, a. J., Berrisford, P., Poli, P., Kobayashi, S.,
 603 ... Vitart, F. (2011, apr). The ERA-Interim reanalysis: configuration and
 604 performance of the data assimilation system. *Quarterly Journal of the Royal*
 605 *Meteorological Society*, *137*(656), 553–597. doi: 10.1002/qj.828
- 606 Dill, R. (2008). *Hydrological model LSDM for operational Earth rotation and gravity*
 607 *field variations* (STR 08/09). Potsdam: GFZ. doi: 11.2312/GFZ.b103-08095
- 608 Dobsław, H., & Dill, R. (2018). *Product Description Document* (Vol. 0). doi: 10
 609 .1016/j.asr.2017.11.044.
- 610 Gambis, D., & Bizouard, C. (2009). The Combined Solution C04 for Earth Ori-
 611 entation Parameters Consistent with International Terrestrial Reference Frame
 612 2005. In H. Drewes (Ed.), *Geodetic reference frames* (Vol. 134). Berlin, Heidel-
 613 berg: Springer Berlin Heidelberg.
- 614 Göttl, F., Murböck, M., Schmidt, M., & Seitz, F. (2019). Reducing filter effects
 615 in GRACE-derived polar motion excitations. *Earth, Planets and Space*, *71*(1).
 616 doi: 10.1186/s40623-019-1101-z
- 617 Gross, R. S. (2007). Earth Rotation Variations - Long Period. *Earth*, *11*, 239 – 294.

- 618 Holme, R., & De Viron, O. (2013). Characterization and implications of in-
619 tradecadal variations in length of day. *Nature*, *499*(7457), 202–204. doi:
620 10.1038/nature12282
- 621 Jungclaus, J. H., Fischer, N., Haak, H., Lohmann, K., Marotzke, J., Matei, D., ...
622 Von Storch, J. S. (2013). Characteristics of the ocean simulations in the Max
623 Planck Institute Ocean Model (MPIOM) the ocean component of the MPI-
624 Earth system model. *Journal of Advances in Modeling Earth Systems*, *5*(2),
625 422–446. doi: 10.1002/jame.20023
- 626 Kantha, L. H., Stewart, J. S., & Desai, S. D. (1998). Long-period lunar fort-
627 nightly and monthly ocean tides. *Journal of Geophysical Research C: Oceans*,
628 *103*(3336), 12639–12647. doi: 10.1029/98jc00888
- 629 Mitrovica, J. X., & Wahr, J. (2011). Ice Age Earth Rotation. *Annual Review*
630 *of Earth and Planetary Sciences*, *39*(1), 577–616. doi: 10.1146/annurev-earth
631 -040610-133404
- 632 Nastula, J., & Śliwińska, J. (2020). Prograde and Retrograde Terms of Gravimetric
633 Polar Motion Excitation Estimates from the GRACE Monthly Gravity Field
634 Models. *Remote Sensing*. doi: 10.3390/rs12010138
- 635 Otten, M., Flohrer, C., Springer, T., & Enderle, W. (2012). Multi-technique combi-
636 nation at observation level with NAPEOS. *EGU General Assembly Conference*
637 *Abstracts*, *14*, 7925.
- 638 Petit, G., & Luzum, B. (2010). IERS Conventions 2010. *IERS Technical Note No*
639 *36*.
- 640 Ponte, R. M., & Ali, A. H. (2002). Rapid ocean signals in polar motion and length
641 of day. *Geophysical Research Letters*, *29*(15).
- 642 Ratcliff, J., & Gross, R. S. (2019). *Combinations of Earth Orientation and*
643 *POLE2018* (Tech. Rep. No. October 2019). Jet Propulsion Laboratory,
644 Pasadena, CA.
- 645 Ray, J., Rebeschung, P., & Griffiths, J. (2017, nov). IGS polar motion measurement
646 accuracy. *Geodesy and Geodynamics*, *8*(6), 413–420. doi: 10.1016/j.geog.2017
647 .01.008
- 648 Ron, C., Vondrák, J., Dill, R., & Chapanov, Y. (2019). Combination of geo-magnetic
649 jerks with updated esmgfz effective angular momentum functions for the mod-
650 elling of polar motion excitation. *Acta Geodynamica et Geomaterialia*, *16*(4),
651 359–363. doi: 10.13168/AGG.2019.0030
- 652 Salstein, D. A. (1993). Monitoring atmospheric winds and pressures for Earth ori-
653 entation studies. *Advances in Space Research*, *13*(11), 175–184. doi: 10.1016/
654 0273-1177(93)90220-6
- 655 Seitz, M., Angermann, D., Bloßfeld, M., Drewes, H., & Gerstl, M. (2012). The 2008
656 DGFI realization of the ITRS: DTRF2008. *Journal of Geodesy*, *86*(12), 1097–
657 1123. doi: 10.1007/s00190-012-0567-2
- 658 Śliwińska, J., Nastula, J., Dobslaw, H., & Dill, R. (2020, mar). Evaluating Gravimet-
659 ric Polar Motion Excitation Estimates from the RL06 GRACE Monthly-Mean
660 Gravity Field Models. *Remote Sensing*, *12*(6), 930. doi: 10.3390/rs12060930
- 661 Taylor, K. E. (2001). Summarizing multiple aspects of model performance in a single
662 diagram. *Journal of Geophysical Research*, *106*(D7), 7183–7192. doi: 10.1029/
663 2000JD900719
- 664 Vondrak, J. (1977). Problem of smoothing observational data II. *Bull. Astron.*
665 *Inst. Czech*, *28*, 84–89.
- 666 Wilson, C. R., & Vicente, R. O. (1990). Maximum likelihood estimates of polar
667 motion parameters. *Washington DC American Geophysical Union Geophysical*
668 *Monograph Series*, *-1*, 151–155.
- 669 Yoder, C. F., Williams, J. G., & Parke, M. E. (1981). Tidal Variations of Earth Ro-
670 tation. *Journal of Geophysical Research*, *86*(B2), 881–891.
- 671 Yun, T.-q. (2019). Earthquake Fastens Earth Rotation. *Asian Journal of Geological*
672 *Research*, *2*(1), 1–9.